Photon-Efficient Aberration Correction for 3D-STED Imaging of Thick Biological Specimens Using Sensorless Adaptive Optics

Siqing Dai, Andrei Kobitski, Amirhossein Barati Sedeh, Süheyla Eroğlu-Kayıkçı, Lennart Hilbert, and G. Ulrich Nienhaus*

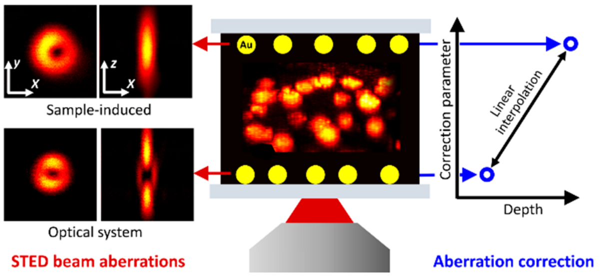

ABSTRACT: Stimulated emission depletion (STED) microscopy is a powerful super-resolution imaging technique for investigating the subcellular structure of biological samples in all three spatial dimensions. Its application to thick specimens is challenging, however, as sample-induced optical aberrations distort the intricate phase patterns of the STED beams and, consequently, their focal intensity distribution. Notably, the central intensity minimum, which is essential for resolution enhancement, is lifted at larger sample depths. Here we present a technique for correction of STED beam aberrations featuring minimal light exposure of the samples to avoid photobleaching and phototoxicity. We quantify STED beam aberrations by using modal wavefront sensing with spatial light modulators (SLMs) as adaptive optics (AO) elements based on reflection imaging of gold beads immobilized at the top and bottom surfaces enclosing the thick (≥100 μm) biological specimen. Based on this information, wavefront aberrations can be successfully compensated for all depths by linear interpolation of the correction parameters. We demonstrate the excellent imaging performance of AO 3D stimulated emission double depletion (STEDD) microscopy on cell nuclei of zebrafish embryos.

KEYWORDS: *super-resolution microscopy, deep tissue imaging, STED microscopy, aberration correction, sensorless adaptive optics*

INTRODUCTION

Far-field optical florescence microscopy is a powerful method for the study of the structure and dynamics of biological specimens, thanks to the availability of a wide range of sophisticated methods for attaching fluorophores to structures of interest with molecular specificity and selectivity.[1,2] In recent years, intriguing super-resolution fluorescence imaging techniques have come to widespread use,[3−6] circumventing the Abbe diffraction barrier and offering insights into subcellular structures all the way down to the molecular scale. Among these, stimulated emission depletion (STED) microscopy uses two spatially and temporally superimposed focused laser beams as a raster-scanning probe in a confocal microscope. In the sample, fluorophores are locally excited by a Gaussian beam focused into a diffraction-limited spot. The second (depletion, or "STED") beam, which has a wavelength in the red tail of the fluorescence emission band, is phase-modulated so that it features a central intensity minimum (ideally zero intensity).[7] Its high intensity ($10^2 - 10^3$ MW/cm^2) ensures stimulated emission of all fluorophores except those located next to the central minimum and thereby generates a greatly reduced effective scanning spot. Typically, a spatial resolution in the range of a few tens of nanometers can be achieved in the two lateral dimensions with a so-called "donut" depletion beam (2D-STED), and in the axial dimension with a "bottle" depletion beam (z-STED). For three-dimensional (3D) STED imaging, the two STED beams are usually applied in combination.

The STED image resolution is theoretically unlimited and can be finely tuned via the power of the depletion beam. In practice, however, the resolving power crucially depends on the quality of the intensity minimum of the depletion beam, which can greatly deteriorate in the presence of system- and sample-induced aberrations.[8] Indeed, the highly heterogeneous optical properties of biological tissues (Figure 1a) can lead to severely distorted wavefronts (Figure 1b) and, consequently, STED imaging deeper into specimens (>30 μm) is a challenging task. While the donut depletion point spread function (PSF, generated by a vortex phase plate) shows a certain degree of robustness against aberrations,[9] the bottle depletion beam PSF (generated by a π-step cylindrical, or "top-hat", phase mask) is exquisitely sensitive to aberrations,[10−12] up to the point that the central intensity minimum disappears completely (Figure 1c).

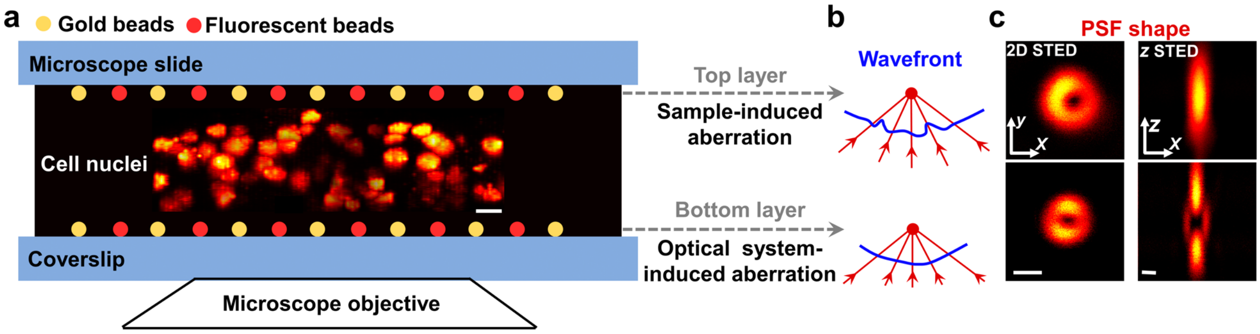

Figure 1. STED imaging of zebrafish embryo samples in the presence of depletion beam aberrations induced by the optical system and the sample. (a) Schematic depiction of a sandwich sample, consisting of bottom and top layers of gold and/or fluorescent nanobeads attached to glass and a specimen (e.g., zebrafish embryo animal cap) in-between, mounted on the inverted microscope. (b) Illustration of depth-dependent aberrations: at the bottom surface, there are small wavefront distortions induced by the optical elements; inside the specimen, wavefront distortions increase with depth due to index mismatch and variations. (c) 2D- and *z*-STED depletion beam PSFs at the bottom and top surfaces, measured with gold beads. Scale bars: (a) 10 and (c) 0.3 μm.

Recent years have seen considerable efforts expended on the compensation of optical aberrations in STED microscopy by predistorting the wavefronts using adaptive optics (AO) to create the optimal depletion beam PSF deep inside aberrating samples.[10−19] To this end, spatial light modulators (SLMs) have been widely employed as versatile devices not only for shaping the depletion beam PSF, but also for wavefront correction.[10−12,14,17−19] In sensorless modal AO,[20] aberrations are conveniently modeled by a set of mutually independent (Zernike) modes, the amplitudes of which are varied to examine their effects on the image, as judged by a suitable image quality metric based on, e.g., image intensity,[10,12,17,19] image sharpness,[10] Fourier ring correlation (FRC),[14] or fluorescence correlation spectroscopy (FCS).[11] Consequently, aberrations can be compensated for by predistorting the wavefront accordingly. However, all STED imaging-based AO implementations require hundreds or even thousands of exposures for aberration correction, resulting in sample deterioration due to photobleaching and phototoxicity. In our ongoing research, we aim to visualize and quantify the localization of RNA polymerase II (Pol II) clusters forming close to transcriptionally active genes in the cell nuclei of zebrafish embryos with nanoscale resolution.[21] To this end, embryonal tissues (animal caps) are fixed at the sphere stage of development, immunolabeled with the dye STAR RED (Abberior, Göttingen, Germany) using antibodies against Pol II, and immersed in a glycerol/water mixture (70/30, by volume). For imaging, we employ three-dimensional stimulated emission double depletion (3D STEDD) microscopy, a STED variant that enables background-free super-resolution imaging.[22,23] In our densely stained, ∼100 μm thick samples, the STEDD image quality was found to deteriorate markedly with increasing depth due to sample-induced aberrations.[24] Therefore, we have developed a robust and photon-efficient AO strategy for precompensation of STED beam aberrations within these tissue samples. Unlike other AO implementations,[10−20] we do not expose the sample to the powerful STED beam but rather exploit the strong light scattering from gold beads. In a sandwich structure (Figure 1a), we measure the light reflected from immobilized gold beads (80 nm ⌀) before and after passing through the sample. We decompose the aberrated wavefront in terms of the Zernike modes and systematically vary their coefficients. By comparing experimental and theoretical (ideal) PSF shapes using cross-correlation, we identify optimal parameters for wavefront precompensation. Furthermore, we demonstrate that linear interpolation between the coefficients at zero and maximum depths yields reliable estimates of precompensation parameters for arbitrary sample depths. Our reflection imaging-based procedure minimizes light exposure and thus causes negligible irradiation-induced sample deterioration (photobleaching, phototoxicity) and allows for 3D STEDD imaging of zebrafish embryo specimens with nearly depth-independent image quality.

RESULTS AND DISCUSSION

PSF-Based Correction of STED Beam Aberrations. We examine system- and sample-induced aberrations of the depletion beams based on modal wavefront sensing. Deviations from the ideal wavefront are expanded in a series of Zernike modes, Z_n^m, which are defined on a unit circle with radius, ρ, and azimuth, θ, as coordinates, having coefficients, C_n^m,

$$\Psi(\rho, \theta) = \sum_{n,m} C_n^m Z_n^m(\rho, \theta) \tag{1}$$

Zernike polynomials are advantageous in this context, as they are orthogonal and represent distinct optical aberrations in the paraxial approximation.[25] However, coupling between modes occurs when using high-NA objectives. We systematically vary the C_n^m values by loading the corresponding phase patterns onto the two SLMs for modulation of the 2D-STED and *z*-STED beams and study their effects on the PSFs. The PSFs are experimentally assessed by imaging individual gold nanobeads attached to the bottom and top surfaces of the sample sandwich (Figure 1a), which strongly scatter light upon focused irradiation with the modulated 2D-STED and *z*-STED beams. As a quality metric, we calculate the cross-correlation function (CC) between the measured and theoretical PSFs, which reveals their degree of similarity,

$$CC = \frac{\sum_{m,n}(A_{mn} - \bar{A})(B_{mn} - \bar{B})}{\sqrt{\sum_{m,n}(A_{mn} - \bar{A})^2 \sum_{m,n}(B_{mn} - \bar{B})^2}} \tag{2}$$

Here, A_{mn} and B_{mn} are the intensities of pixels with indices m and n, associated with the calculated and measured foci, respectively; overlines indicate averages. Prior to the CC calculation, the experimental PSF is centered and normalized. To achieve the largest CC value, and thus a minimally distorted

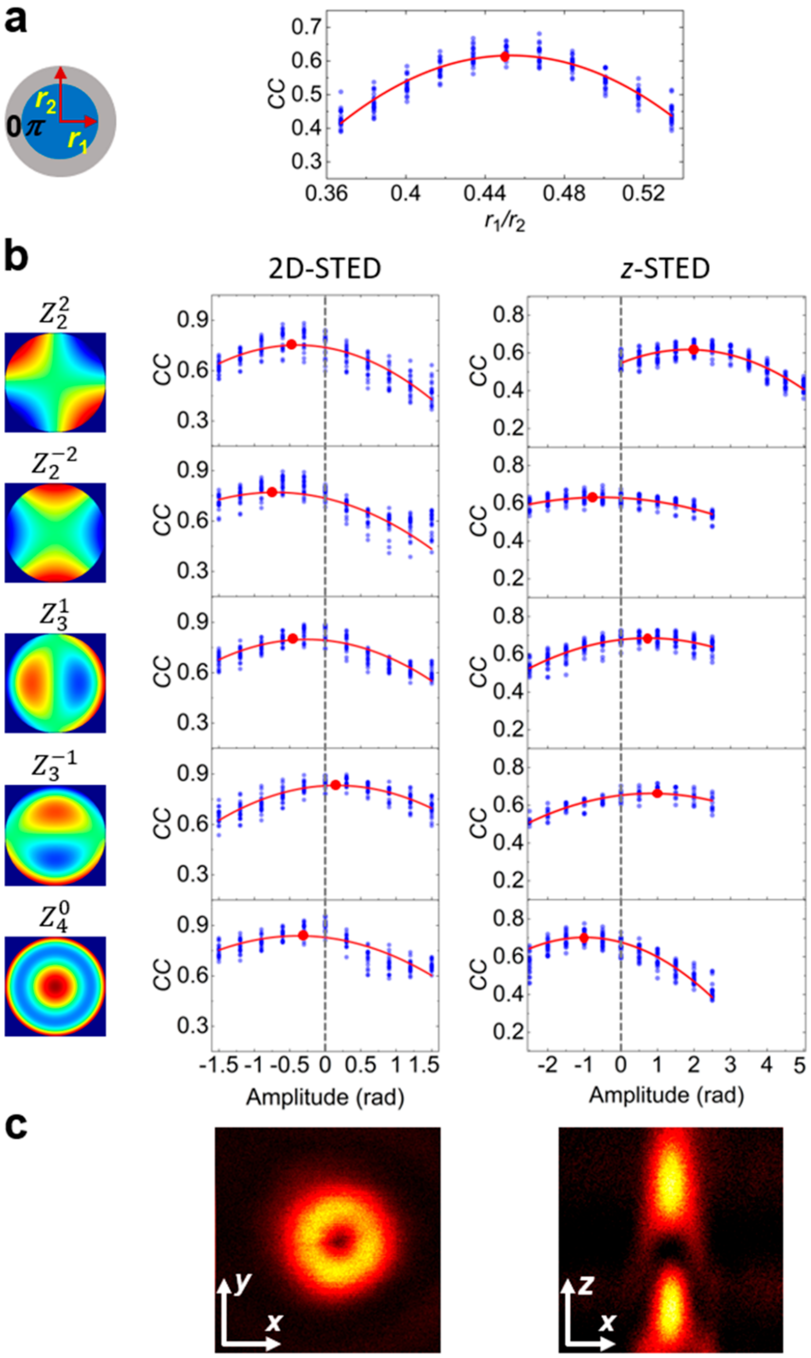

Figure 2. Quantitative characterization of sample-induced aberrations in 2D- and *z*-STED beams at a depth of 110 μm. (a) Optimization of the π/0-phase radius ratio of the cylinder phase mask (left) used for the bottle (*z*-STED) beam. Right: cross-correlation (CC) data (blue dots), calculated for individual gold beads (80 nm ⌀) as a function of r_1/r_2. Also shown is a fit of all data with a parabola (red line); its maximum corresponds to the best-fit r_1/r_2 value (red dot). (b) Sequential optimization of the Zernike mode amplitudes. Left: illustrations of the polynomials describing primary aberrations (astigmatism: Z_2^2, Z_2^{-2}; coma: Z_3^1, Z_3^{-1}; primary spherical aberration: Z_4^0). CC data of the 2D- (middle) and *z*-STED (right) PSFs displayed as in panel (a). (c) Cross sections of 2D-STED and *z*-STED PSFs with compensated aberrations measured on a single gold bead.

bead image, we change the beam phase systematically by applying Zernike modes corresponding to the primary aberrations, namely astigmatism (Z_2^2, Z_2^{-2}), coma (Z_3^1, Z_3^{-1}), and primary spherical aberration (Z_4^0), as they are the most relevant modes in this context.[8,11] When using high-NA objectives, one needs to account for the strong couplings between horizontal coma (Z_3^1) and tip (Z_1^1), vertical coma (Z_3^{-1}), and tilt (Z_1^{-1}), and further between the primary spherical mode (Z_4^0) and defocus (Z_2^0).[26] These intrinsic couplings of primary aberration modes to displacement modes are detrimental for STED microscopy, as they generate mutual displacements of the excitation and depletion foci. Thus, we have quantified the PSF shift as a function of the ratio between aberration and displacement modes (Supporting Information, Note 1, Figure S1). Based on this knowledge, we always apply combinations of the coupled Zernike modes with amplitude ratios that minimize the shift. In addition to the Zernike mode coefficients, the radius ratio, r_1/r_2, of the π- and 0-phase

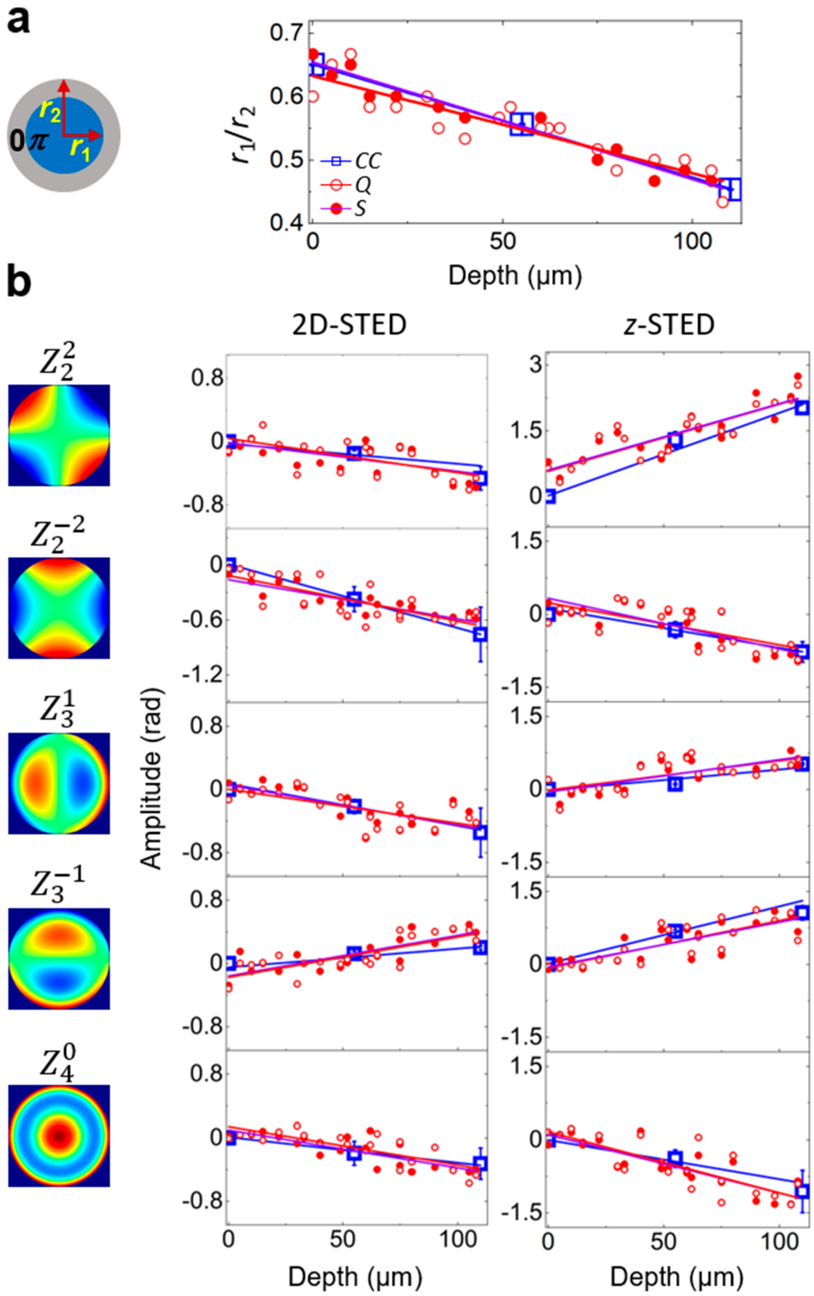

Figure 3. Depth dependence of optimized aberration correction parameters. (a) Optimization of the $\pi/0$-phase radius ratio of the cylinder phase mask (left) used for the bottle (z-STED) beam. Right: Optimal $\pi/0$-phase radius ratios of the cylinder phase mask determined with cross-correlation (CC) metrics on gold bead samples, and quadratic (Q) and sharpness (S) metrics on fluorescent DRB samples, plotted as a function of imaging depth. (b) Left: illustrations of the Zernike polynomials describing primary aberrations. Right: Optimized mode amplitudes are plotted as a function of imaging depth. Types and colors of symbols and best-fit lines are as shown in the inset of panel (a).

circular regions in the cylinder phase pattern, which controls the intensity minimum of the z-STED beam focus, is a crucial parameter that needs to be examined.

We start the aberration correction with measurements at the lower surface of the sample compartment (i.e., above the coverslip) to compensate for microscope system aberrations (Table S1). The resulting phase patterns are loaded onto the corresponding SLMs and, subsequently, the phases for correction of sample-induced aberrations, which are determined at the upper surface (i.e., at maximum sample depth), are added on top. For parameter optimization, gold beads are imaged at several mode amplitudes and all CC data points are fitted with a parabolic function to localize the maximum. Ideally, one could measure each Zernike mode independently until the set of amplitudes for correction is complete. However, in practice, the signal-to-noise ratio deteriorates for larger aberrations, resulting in dimmer images. Therefore, to minimize uncertainties as well as crosstalk between modes,[14] we determine optimal Zernike mode amplitudes in the sequence: astigmatism, coma and primary spherical aberrations, always keeping the values found for the prior modes.

In Figure 2, we illustrate our AO strategy with data for the 2D-STED and z-STED PSF optimization at the upper surface, i.e., at a depth of 110 μm. For the z-STED beam, it is crucial to begin by optimizing the radius ratio, r_1/r_2, of the π- and 0-phase regions in the cylinder phase pattern, to establish complete destructive interference in the center (Figure 2a).[27] This parameter depends on the width of the STED beam in relation to the back-aperture size of the objective. In our high-NA microscope system, it decreases from 0.65 at zero depth to 0.45 at 110 μm. After this step, we systematically investigated the contributions of the various Zernike modes to the distortion of the 2D-STED and z-STED PSFs. The z-STED beam is more susceptible to aberrations than the 2D-STED beam, as inferred from the optimal mode amplitudes of Z_2^2, Z_2^{-2}, Z_3^1, Z_3^{-1}, and Z_4^0 (Figure 2b).

After wavefront correction, the PSF quality of both STED foci was greatly improved (compare Figure 2c and 1c, upper row) yet not completely restored to the shapes at zero depth (Figure 1c, bottom row). Thus, we asked if repeating the optimization procedure for another round would lead to a further improvement. However, we found the same Zernike mode amplitudes within the errors, implying that further crosstalk between the investigated modes was insignificant (Figure S2 and Table S2). We also tested if additional Zernike modes might further improve the PSF quality of the z-STED beam (Figure S3), namely, trefoil (Z_3^3, Z_3^{-3}) and second and third order spherical aberrations (Z_6^0 and Z_8^0, respectively). While trefoil aberrations had no effect on the PSF whatsoever, Z_6^0 and Z_8^0 had nearly optimal amplitudes without correction. The relative contributions of all parameters included in PSF optimization are given in Table S3. Taken together, our results suggest that restoring the PSF at a depth of 110 μm is limited by other factors than STED beam wavefront distortions (detection beam aberrations, photon scattering, and absorption).

We have implemented a fully automated protocol for the rapid determination of the parameters for aberration correction. The entire procedure takes only a few minutes and thus can easily be carried out for each new sample mounted on the microscope.

Depth Dependence of Sample-Induced Aberration Correction Parameters. Aberrations increase continuously with imaging depth in specimens lacking abrupt changes in refractive index including biological tissues,[28,29] suggesting that a linear variation of the parameters may yield a satisfactory first-order correction.[30] To assess the validity of this approximation, we investigated the 2D-STED and z-STED PSF aberrations, assessed by reflection imaging of gold beads, also in a sandwich sample with a spacing of 55 μm rather than 110 μm between the coverslip and the microscope slide (Figure S4). Overall, the aberration data at 55-μm thickness (Figure S4) look qualitatively similar to those at 110 μm (Figure 2), with changes of the parameters for best correction about half of those at 110 μm. This is clearly seen in Figure 3, where the gold bead reflection data (blue) at 0, 55, and 110 μm are plotted against the depth, confirming a close-to linear variation of the optimal phase plate $\pi/0$ radius ratio and Zernike mode amplitudes with depth; the slopes are given in Table S4.

Next, we asked if this linear dependence also extends to STED fluorescence imaging. To this end, we prepared a phantom sample of 110 μm thickness consisting of dark red fluorescent beads (DRBs, 40 nm ⌀) homogeneously distributed throughout the volume by immobilization in a transparent agarose gel. A 3D-STED image of a single DRB represents an effective PSF, which suffers from broadening and brightness reduction in the presence of STED beam aberrations. Accordingly, we employed sharpness as well as intensity-squared metrics (Supporting Information, Note 2)[10] to determine correction values for the $\pi/0$ radius ratio and the Zernike mode amplitudes from images of individual beads. In Figure 3, these data (red circles) are included in the plots of the gold bead data (blue squares). Notably, the larger scatter of the DRB data points is due to the lower signal-to-noise ratio of the fluorescence images. The overall trends of both data sets are similar, and the linear regressions essentially agree with the experimental uncertainties.

We conclude that the reflection imaging of gold beads allows STED beam wavefront optimization for 3D-STED imaging with minimal light exposure. Moreover, a simple linear interpolation of parameters taken at zero and maximum depth allows a correction for arbitrary depths within the sandwich sample. Thus, we achieve an STED beam aberration correction with minimal light exposure of the sample.

Performance Assessment of Linear Interpolation of Correction Parameters. To evaluate the feasibility of linear interpolation of STED PSF-based parameters to compensate for aberrations at different depths, we compared images of DRBs in a bead phantom sample as a function of depth, acquired using standard confocal, conventional 3D-STED and AO 3D-STED modalities. For consistency, we kept the excitation power constant at 3.8 μW. Figure 4a shows exemplary xz-sections taken for identical lateral positions at depths of 10, 40, 70, and 100 μm. Visual inspection of the confocal images reveals an increasing blurriness of the spots with depth. As expected, the spots are sharper in the STED image at 10 μm but fade at greater depth as a result of STED beam aberrations that lift the central intensity minimum. By contrast, sharp spots are visible at all depths for AO STED based on linear interpolation of the parameters obtained from gold bead reflections.

For quantitative analysis, we fitted individual bead images with 2D Gaussian functions to extract the full width at half-maximum (fwhm) along the z-axis and the total intensity (Figure 4b). In confocal imaging, the DRB spots get broader and dimmer with increasing depth due to aberrations in the excitation and detection paths, and image resolution and contrast deteriorate continually. The STED data feature an enhanced axial resolution with respect to confocal imaging and an essentially constant intensity, but only up to a depth of ~25 μm. Beyond this point, aberrations of the STED beams are so severe that the resolution enhancement disappears, and the bead intensity approaches the noise floor. In the absence of deep central intensity minima, the focused STED beams just produce an indiscriminate intensity depletion. In stark contrast, the AO STED images exhibit only a moderate deterioration of the axial resolution, as judged from the fwhm, and less intensity degradation, maintaining superior performance over confocal microscopy at all depths.

To examine the effect of the aberration correction on the lateral and axial STED resolution separately, we imaged the DRBs in our phantom sample as a function of the depletion power. Lateral and axial fwhm data from individual beads are shown in Figure 5 for conventional STED at 110 μm and AO STED at 0 and 110 μm. AO corrections have only a moderate impact on the lateral resolution (e.g., 105 ± 40 vs 90 ± 21 nm for STED and AO STED, respectively, at 110 μm depth and 100 mW STED power), reflecting the resistance of the 2D-STED vortex beam to aberrations. Nonetheless, compensating

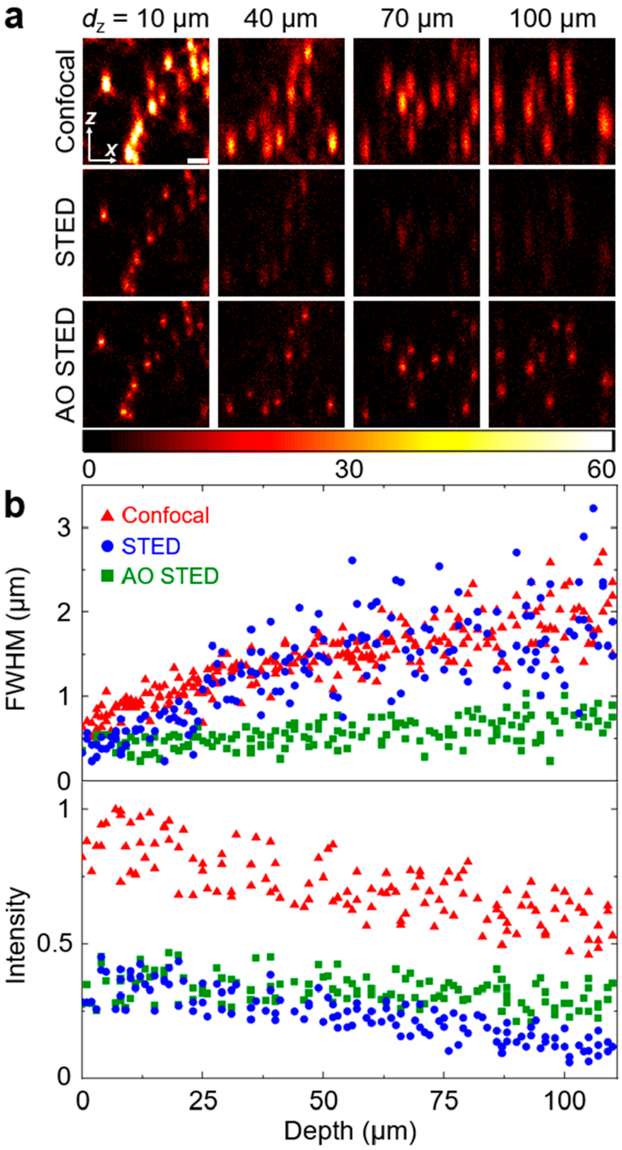

Figure 4. Quality assessment of confocal, regular STED, and AO STED modalities by analyzing images of immobilized DRBs at different depths. Images were taken with 3.8 *μ*W of 640 nm excitation light, and 60 and 30 mW for the 2D-STED and *z*-STED beams, respectively. (a) *xz*-images of beads at depths (middle of the shown *z*-range) of 10, 40, 70, and 100 *μ*m; scale bar, 1 *μ*m. (b) For individual DRBs imaged with the three imaging modalities (colors as shown in the inset), fwhm (top panel) along the axial direction and intensities (bottom panel) are plotted as a function of depth.

for these aberrations still enhances the lateral resolution significantly at all depths, bringing the data close to the values at zero depth (69 ± 15 nm at 100 mW power). By contrast, the correction has a striking impact on the axial resolution. It is clear that, without correction, aberrations completely ruin the *z*-STED beam resolution enhancement over the entire range of STED beam powers.

We further investigated the axial resolution achievable with AO STED in the DRB phantom sample at four different depths (Figure S6). In this experiment, we maintained a constant overall bead intensity in the AO STED image at all depths by readjusting the 640 nm laser power. This strategy counteracts aberrations in the excitation beam, as its focal broadening leaves fewer undepleted fluorophores in the central region. At a depth of 110 *μ*m, the axial resolution was 3-fold enhanced for AO STED over confocal imaging (398 ± 45 nm vs 1199 ± 63 nm). Although comparisons with literature data should be taken with a grain of salt, as they depend on measurement conditions, including specimen, depth, laser power, and analysis method, our axial resolution at 80 *μ*m depth (309 nm) agrees with previously reported data (310 nm[12]) at the same depth.

Imaging Animal Caps of Zebrafish Embryos with AO 3D-STEDD Nanoscopy. Next, we applied AO 3D-STEDD nanoscopy with a linear depth dependence of the 2D-STED and *z*-STED PSF correction parameters to the imaging of cell nuclei in animal caps of zebrafish embryos. In addition, we acquired standard confocal and conventional 3D-STED and 3D-STEDD images (without AO) for comparison. An illustrative 3D rendering of an individual nucleus centered 96 *μ*m from the coverslip is displayed in Figure 6a. The bright fluorescent spots, corresponding to Pol II clusters formed in the vicinity of regulatory genomic elements,[21] are not well separated in the confocal image. By contrast, they are well resolved by AO STEDD but not by STEDD without aberration correction.

In Figure 6b, we present *xy*-, *xz*-, and *yz*-sections through the nucleus shown in Figure 6a to visualize the differences between the imaging modalities. Again, while the confocal sections are quite blurry, AO 3D-STED images are somewhat better resolved and AO 3D-STEDD images are very well resolved in the lateral plane. Notably, the high background due to nondepleted fluorescence in the confocal volume and fluorescence re-excitation by the depletion beam in the STED images is effectively removed by the STEDD method.[21,22,24] This is also clearly visible in the line profiles (Figure 6c), which further show that the AO 3D-STEDD images provide excellent axial resolution at larger depths.

For further assessment of the image quality, we analyzed images taken on cell nuclei positioned at various depths using decorrelation analysis.[32] This approach extracts the particular spatial frequency in the Fourier-transformed image above which the object signal amplitude becomes smaller than the noise, which can be recast into a characteristic size, serving as a measure of resolution. For this analysis, we took *xy*-sections of cell nuclei; exemplary images are shown in Figure S5. The characteristic size of Pol II clusters at small depth (Figure 7) is in a good agreement with earlier microscopy data,[21] and the depth dependence is similar to the one observed for the DRB data in Figure 4. The confocal resolution degrades gradually with increasing depth due to aberrations in the excitation and detection paths. The 3D-STEDD resolution deteriorates drastically at small depths and exceeds the confocal resolution above 30 *μ*m, which is a consequence of poorer photon statistics due to (aberrated) depletion and background subtraction. By contrast, the characteristic object size in the AO 3D-STEDD image remains markedly smaller than the confocal one at all depths.

Finally, we address the crucial issue of minimizing light exposure of delicate biological specimens, such as our zebrafish embryos. Photobleaching and phototoxicity (in live specimens) is of great concern in STED fluorescence image-based AO optimization, especially in closed-loop implementations, which involve repetitive beam optimization steps with long exposures of the sample to the strong STED beam.[10−12,14,17,30] With a power density of up to 1 GW cm^{-2}, the depletion beam does not only de-excite electronically excited fluorophores (in

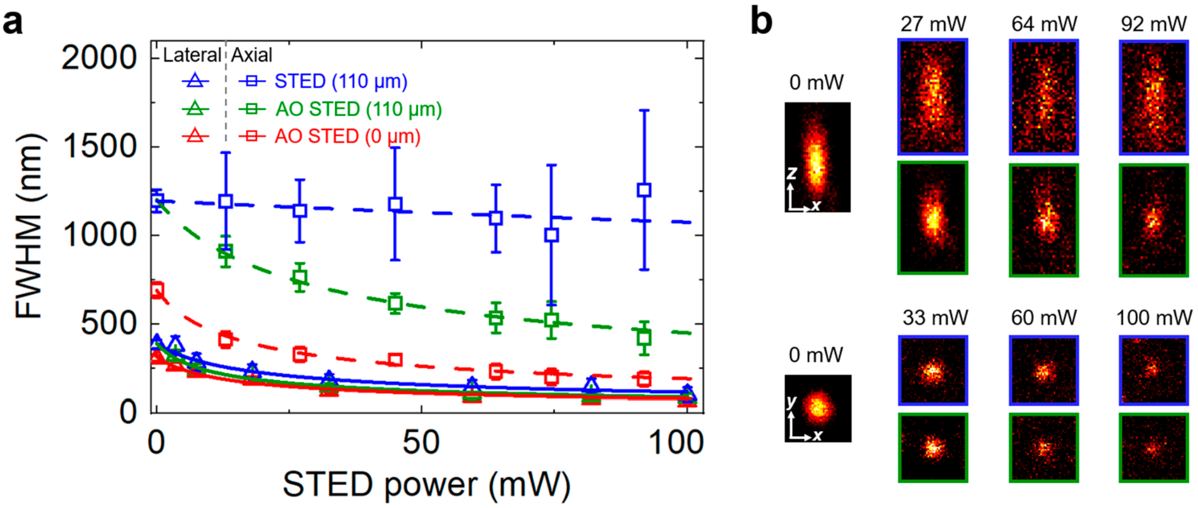

Figure 5. Lateral and axial resolution in STED and AO STED modalities at various depletion powers. Data were taken with 3.8 and 7.6 μW of 640 nm excitation light at depths of 0 and 110 μm, respectively. (a) Lateral (triangles, solid lines) and axial (squares, dashed lines) resolutions in STED at 110 μm (blue) and AO STED at 0 (red) and 110 μm (green) depths versus STED power. Lines are fits with the STED resolution equation.[31] (b) Exemplary STED (blue frames) and AO STED (green frames) *xy*- and *xz*-images of a bead captured with different depletion powers.

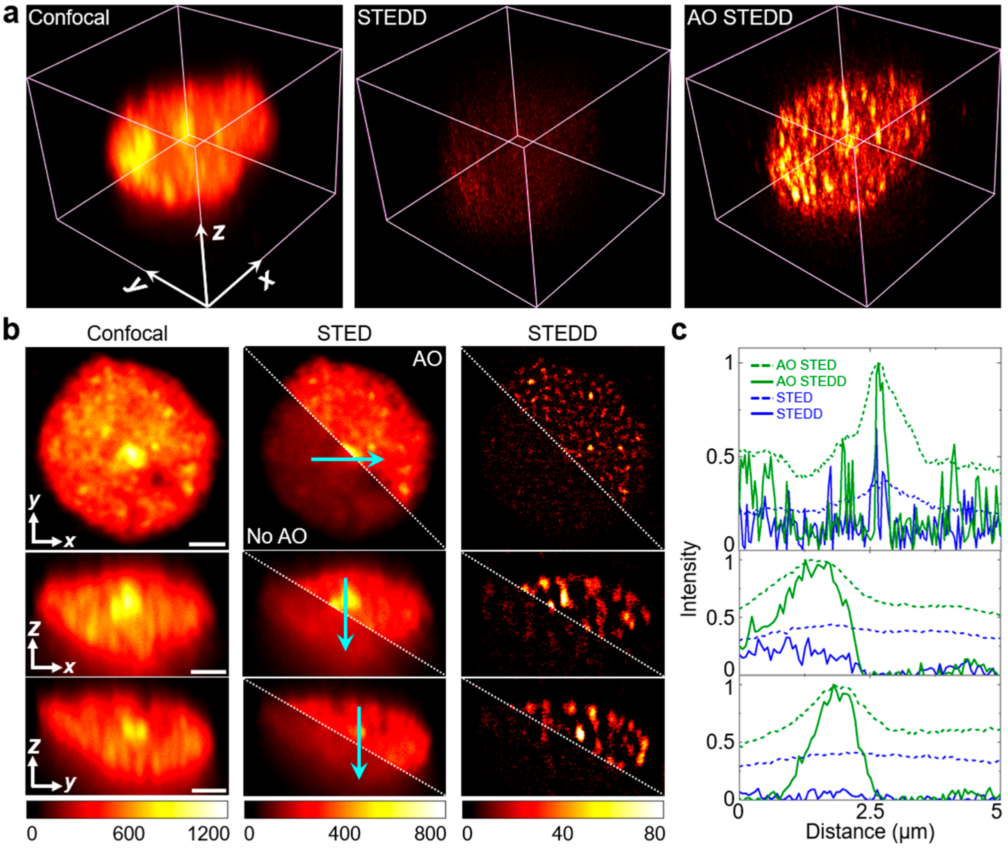

Figure 6. Fluorescence images of a cell nucleus of a zebrafish embryo located 96 μm from the coverslip. (a) Renderings of 3D image stacks are shown with the same brightness scale. They were acquired with confocal, 3D-STEDD and AO 3D-STEDD microscopy modalities, covering a volume of $12.6 \times 12.6 \times 9.8\ \mu\text{m}^3$ (250×250 pixels, 40 frames). (b) Lateral (*xy*) and axial (*xz*, *yz*) single-plane sections through the centers of the nucleus shown in (a); scale bar: 2 μm. The STED and STEDD images are displayed both with (upper right, "AO") and without aberration compensation (lower left, "No AO"). (c) Line profiles along the arrows in the STED images in (b). AO data were normalized to one at the peak; data taken without AO were scaled to the respective AO intensities.

the singlet S_1 state) but also promotes excited fluorophores (singlet S_1 or triplet T_1 states) to even higher and more vulnerable states. Accordingly, the STED imaging-based measurement of parameters for aberration correction inevitably causes significant sample deterioration. Figure S7 shows a typical bleaching response of a zebrafish sample, immunolabeled with STAR RED fluorophores, under relatively mild laser irradiation conditions appropriate for AO parameter acquis-

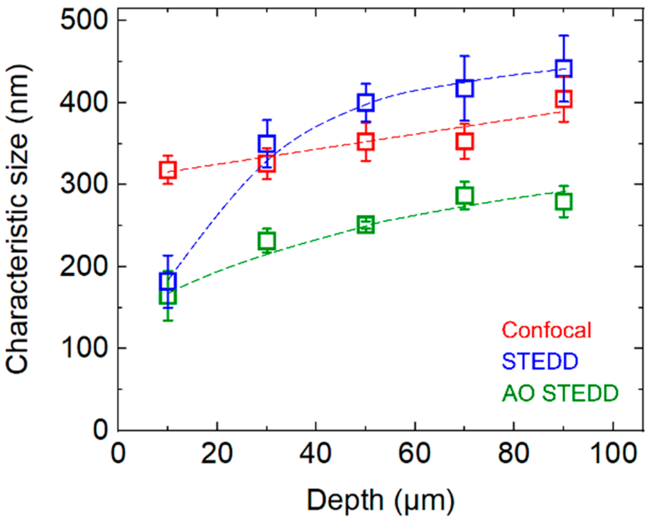

Figure 7. Quantitative assessment of the characteristic size of Pol II clusters in the cell nuclei of zebrafish embryos at different depths. Decorrelation analysis was performed on *xy*-sections (15.2 × 15.2 μm^2) acquired by using confocal, 3D-STEDD and AO 3D-STEDD imaging. Dashed lines are shown to guide the eye.

ition. Of note, although STAR RED rhodamine-based fluorophores are highly photostable, the overall fluorescence is down by a factor of 2 after collecting a few hundred frames. By contrast, reflection imaging of gold nanobeads requires only a few microwatts (4 μW used here) of STED beam power, more than 4 orders of magnitude below the power used for depletion. Importantly, the fluorophores are not resonantly excited in this imaging mode, as the 640 nm excitation beam is off and the near-infrared (NIR) STED beam wavelength (779 nm) could only excite fluorophores via two-photon excitation, which is negligible for irradiation with focused microwatt beams.

Taken together, precompensating wavefront distortions in the STED beam based on PSF analysis of gold bead reflection images at minimal and maximal sample depth, and a simple linear interpolation in-between, effectively remove aberrations and maintain the excellent resolving power of STED microscopy at all depths. Importantly, minimal light exposure by weak NIR irradiation avoids photobleaching of the sample.

CONCLUSIONS

In recent years, STED microscopy has been widely established as a powerful technique for the 3D super-resolution imaging of subcellular biological structures. However, its performance drastically deteriorates with imaging depth (Figure 7), so that deep imaging of multicellular and tissue specimens has been limited.

Here, we have introduced an AO-based modal wavefront sensing strategy for correction of optical aberrations, enabling 3D-STED imaging deep inside thick (≥100 μm) biological specimens. Our method greatly extends the range of potential biological samples suitable for STED imaging, and we are confident that high-quality images can be acquired at even greater depths. Although the STED wavelength is in the weakly absorbing NIR region of the spectrum (~800 nm), STED microscopy causes substantial photobleaching as well as phototoxicity in live samples, due to the required high intensity of the STED beam ($10^2 - 10^3$ MW cm^{-2}).[33] Therefore, we have designed our AO method for minimal light exposure (a few microwatts of NIR light) during wavefront correction, practically excluding fluorescence excitation. We prepare our samples between two glass surfaces decorated with gold nanobeads serving as strongly scattering fiducial markers and collect reflection images to quantify wavefront distortions. Measurements at zero depth reveal system aberrations, whereas those at maximum depth include sample-induced aberrations. A fully automated measurement protocol enables aberration correction within minutes of imaging a sample. Importantly, by using zebrafish embryo samples as typical biological specimens, we have shown that linear interpolation of the aberration parameters allows us to correct the wavefronts of the STED beams at arbitrary depths between the two boundary surfaces. Notably, this approach has its limits and will not work for samples with strongly heterogeneous index. Altogether, our method is photon-efficient and does not require (possibly multiple) exposures with full beam power, unlike approaches using fluorescence image-based metrics.

So far, we have limited our AO efforts to compensating wavefront distortions to the 2D-STED and *z*-STED beams, which are used in combination for 3D-STED microscopy, resulting in large improvements in the image quality of 3D-STEDD images at a large depth (≥100 μm). However, the excitation and detection beams suffer from optical aberrations as well, as is evident from the deterioration of the resolving power observed in the confocal mode in Figure 7. Future work will address these issues with AO-based techniques to further enhance our STED imaging capabilities.

EXPERIMENTAL METHODS

Sample Preparation. Zebrafish embryo animal caps were prepared as described.[21,24] Briefly, zebrafish embryos were collected ~4 h after fertilization and fixed with 0.3× Danieau's medium mixed with 2% formaldehyde and 0.2% Tween-20 for 45 min at room temperature. After permeabilization and yolk removal, the animal caps were immunostained with antibodies against recruited RNA Pol II molecules, which carry a phosphorylation mark at serine 5, and mounted in a glycerol/water solvent (70/30 v/v).

Sandwich samples containing animal caps of zebrafish embryos, as shown in Figure 1 were prepared as follows. Microscope slides and coverslips (#1.5) were coated with poly-L-lysine. Subsequently, they were exposed to a dilute solution of gold nanobeads (80 nm ⌀, EM.GC80/7, BBI Solutions) and DRBs (40 nm ⌀, 660/680 FluoSpheres, ThermoFisher Scientific) and thoroughly rinsed with Milli-Q water twice in succession. We used two rectangular strips of polymer foil (55 ± 3 or 110 ± 5 μm thickness) as calibrated spacers between the coated glass surfaces. These strips were attached to the microscope slide side by side, forming a 2 mm wide channel in-between. Animal caps immersed in mounting medium (~10 μL) were pipetted into the channel, which was subsequently closed by the coverslip. The whole sandwich assembly was glued together and sealed with nail polish.

The phantom sample with DRBs immobilized in an agarose gel was prepared in the following way. DRB stock solution was added to glycerol in a volume ratio of 1:1000 and mixed thoroughly. Agarose (A6560, Sigma-Aldrich) was dissolved in Milli-Q water (5% w/v) and heated to 70 °C for 40 min. After the DRB and agarose solutions were thoroughly mixed in a volume ratio of 70/30, resulting in a total agarose concentration of 1.5% (w/v), the sample was loaded between a microscope slide and a coverslip as described for the animal cap samples.

STED Microscopy Setup. Confocal and STED images were acquired with our custom-built STEDD microscope,[22] which was modified as depicted in Figure S8. The system is built around a Leica DMi8 inverted microscope body frame. All images were acquired with a HC PL Apo 100×/1.40 oil CS2 objective (Leica, Wetzlar, Germany) having a working distance of 130 μm. Three separate depletion beams (2D-STED, z-STED and Gaussian STED) are derived from a 779 nm beam from a pulsed Ti:Sa laser (Mai Tai HP, Newport Spectra-Physics, Darmstadt, Germany) operating at 80 MHz. Two spatial light modulators (SLM, LETO-3-VIS-009, HOLOEYE Photonics AG, Berlin, Germany) modulate the phase of the 2D-STED (SLM 1) and z-STED (SLM 2) beams (Figure S8). To suppress diffuse reflections, the SLMs were aligned to reflect the first diffraction order of a blazed grating superimposed on the desired phase pattern. Additionally, a vortex phase plate (VPP-1c, RPC Photonics, Rochester, NY) in the 2D-STED beam path ensured a high-quality donut-shaped beam pattern at the focal plane. Therefore, SLM 1 is used solely for aberration corrections, while SLM 2 produces both the cylindrical phase mask of the bottle beam and the phase distribution (eq 1) for aberration correction. The STED beams are split and rejoined by pairs of polarizing beam splitters (PBS) and nonpolarizing beam splitters (BS). To prevent damage to the SLMs, the average laser power on each SLM should be less than 200 mW according to the manufacturer's specifications. The z-STED beam (axial depletion) requires less power at the focal point for efficient depletion than the 2D-STED beam (lateral depletion). The Gaussian STED beam, delayed by 4.5 ns from the 2D-STED and z-STED beams, depletes super-resolved image content to generate a background image in the STEDD approach and needs only 10% of the power of the other two STED beams. Consequently, at the sample, maximum powers of 75 mW for the 2D-STED, 33 mW for the z-STED beam, and 8 mW for the Gaussian STED beam are achieved in the optimal combination of all three STED beams (Figure S8). For fluorescence excitation, blue (470 nm), green (560 nm), and red (640 nm) beams from picosecond-pulsed lasers (LDH-P-C-470B, LDH-D-TA-560B, and LDH-P-C-640B, respectively; all PicoQuant, Berlin, Germany) are combined and introduced into the main excitation beam path using a quad-band dichroic mirror (ZT405/488/561/640rpc −3 mm, Chroma, Bellows Falls, VT). A short-pass dichroic mirror (Z730sprdc, Chroma) combines the excitation and STED beams into one path. The delay between the excitation and the 2D-STED and z-STED beams is set to 200 ps by using a home-built sync/delay electronic device. Fluorescence photons, filtered by a short-pass filter (SPF, FF01−715/SP-25, Semrock, Rochester, NY) and a band-pass filter (BPF, FF02-675/67-25, Semrock), are detected using avalanche photodiodes and recorded with a time-correlated single-photon counting (TCSPC) module (MultiHarp 150P, PicoQuant). Galvanometric scanners (Yanus V, Till Photonics, Gräfelfing, Germany) and a piezo stage (Nano-F100, Mad City Laboratories, Madison, WI) enable precise lateral and axial positioning of the observation volume within the sample. Hardware control during automatic image acquisition as well as data analysis was performed using custom software written in Matlab (MathWorks, Natick, MA).

Image Acquisition and Data Analysis. Lateral and axial STED PSF cross sections were obtained by collecting scattered 779 nm (4 μW) light (without filters in the detection path) from individual 80 nm gold nanobeads through scanning of xy-planes (200 × 200 pixels, 3 × 3 μm^2, 20 μs pixel dwell time) and xz-planes (200 × 200 pixels, 4 × 5 μm^2, 20 μs pixel dwell time). For optimization of the aberration parameters ($\pi/0$ phase plate radius ratio and Zernike modes), we examined 20 gold beads, each at zero and maximum depth. For each aberration parameter, we imaged the beads at 11 different values equally spaced within the relevant range. Each frame was cross-correlated with the corresponding PSF template image, and the cross-correlation amplitudes of each parameter were fitted with a parabolic function; its maximum was taken as the optimal correction value. This procedure was carried out sequentially for the different aberration parameters, and the previously determined optimal values were applied before investigating the next one.

Additionally, optimal wavefront correction parameters were determined with fluorescence imaging of DRBs, using an approach similar to that with the gold nanobeads. For each DRB, two STED images (xy- and xz-sections) were taken with 640 nm fluorescence excitation (3.8 μW), 30 mW of 2D-STED, 15 mW of z-STED power, using a pixel size of 60 × 60 nm^2 (pixel dwell time: 20 μs) and 1× line repetition. To minimize photobleaching, images were acquired at only five different values of each parameter, and intensity-squared and sharpness metrics were used for quality assessment.[10]

Complete 3D stacks of cell nuclei of zebrafish embryos (40 frames of 250 × 250 pixels each, pixel dwell time 20 μs, 3× line repetition) were acquired with a voxel size of 50 × 50 × 250 nm^3, using 1.3 μW of 640 nm laser light for fluorescence excitation, and 60 mW of 2D-STED, 30 mW of z-STED and 6 mW of Gaussian STED beam power.

Single 2D sections of cell nuclei (400 × 400 pixels, 20 μs pixel dwell time, 6× line repetition) were taken with scanning steps of 38 nm (lateral) and 60 nm (axial), using the same laser power as for the 3D stacks.

STEDD images were obtained by subtracting the background image (STED2) from the STED image (STED1) with locally determined weighting factors,[34] using window sizes of 1.5× the fwhm of the confocal PSF. Before subtraction, the STED1 and STED2 images were smoothed with Gaussian filters with standard deviations $\sigma_x = \sigma_y = 0.5$, $\sigma_z = 1$ for the STED1 image (roughly half of the fwhm of the lateral and axial STED PSF), and $\sigma_x = \sigma_y = 4$, $\sigma_z = 10$ for the STED2 image (roughly the fwhm of the lateral and axial confocal PSF).

AUTHOR INFORMATION

Corresponding Author

G. Ulrich Nienhaus − *Institute of Applied Physics, Karlsruhe Institute of Technology, 76131 Karlsruhe, Germany; Institute of Biological and Chemical Systems and Institute of Nanotechnology, Karlsruhe Institute of Technology, 76344 Eggenstein-Leopoldshafen, Germany; Department of Physics, University of Illinois at Urbana−Champaign, Urbana, Illinois 61801, United States;* orcid.org/0000-0002-5027-3192; Email: uli@uiuc.edu

Authors

Siqing Dai − *Institute of Applied Physics, Karlsruhe Institute of Technology, 76131 Karlsruhe, Germany*

Andrei Kobitski − *Institute of Applied Physics, Karlsruhe Institute of Technology, 76131 Karlsruhe, Germany*

Amirhossein Barati Sedeh − *Institute of Applied Physics, Karlsruhe Institute of Technology, 76131 Karlsruhe, Germany*

Süheyla Eroğlu-Kayıkçı − *Institute of Biological and Chemical Systems, Karlsruhe Institute of Technology, 76344 Eggenstein-Leopoldshafen, Germany*

Lennart Hilbert − *Institute of Biological and Chemical Systems, Karlsruhe Institute of Technology, 76344 Eggenstein-Leopoldshafen, Germany; Zoological Institute, Karlsruhe Institute of Technology, 76131 Karlsruhe, Germany*

Funding

This work was funded by the Helmholtz Association, programs Materials Systems Engineering (MSE), Natural, Artificial and Cognitive Information Processing (NACIP), and the Karlsruhe School of Optics and Photonics (KSOP).

Notes

The authors declare no competing financial interest.

REFERENCES

(1) Dean, K. M.; Palmer, A. E. Advances in fluorescence labeling strategies for dynamic cellular imaging. *Nat. Chem. Biol.* **2014**, *10*, 512−523.

(2) Nienhaus, G. U.; Nienhaus, K. Fluorescence labeling. In *Fluorescence microscopy: from principles to biological applications*, Kubitscheck, U., Ed.; Wiley: Weinheim, Germany, 2017; pp 133−164.

(3) Huang, B.; Babcock, H.; Zhuang, X. Breaking the diffraction barrier: super-resolution imaging of cells. *Cell* **2010**, *143*, 1047−1058.

(4) Sahl, S. J.; Hell, S. W.; Jakobs, S. Fluorescence nanoscopy in cell biology. *Nat. Rev. Mol. Cell Biol.* **2017**, *18*, 685−701.

(5) Schermelleh, L.; Heintzmann, R.; Leonhardt, H. A guide to super-resolution fluorescence microscopy. *J. Cell Biol.* **2010**, *190*, 165−175.

(6) Nienhaus, K.; Nienhaus, G. U. Where do we stand with super-resolution optical microscopy? *J. Mol. Biol.* **2016**, *428*, 308−322.

(7) Hell, S. W. Microscopy and its focal switch. *Nat. Methods* **2009**, *6*, 24−32.

(8) Deng, S.; Liu, L.; Cheng, Y.; Li, R.; Xu, Z. Effects of primary aberrations on the fluorescence depletion patterns of STED microscopy. *Opt. Express* **2010**, *18*, 1657−1666.

(9) Deng, S.; Liu, L.; Cheng, Y.; Li, R.; Xu, Z. Investigation of the influence of the aberration induced by a plane interface on STED microscopy. *Opt. Express* **2009**, *17*, 1714−1725.

(10) Gould, T. J.; Burke, D.; Bewersdorf, J.; Booth, M. J. Adaptive optics enables 3D STED microscopy in aberrating specimens. *Opt. Express* **2012**, *20*, 20998−21009.

(11) Barbotin, A.; Galiani, S.; Urbančič, I.; Eggeling, C.; Booth, M. J. Adaptive optics allows STED-FCS measurements in the cytoplasm of living cells. *Opt. Express* **2019**, *27*, 23378−23395.

(12) Zdankowski, P.; Trusiak, M.; McGloin, D.; Swedlow, J. R. Numerically enhanced stimulated emission depletion microscopy with adaptive optics for deep-tissue super-resolved imaging. *ACS Nano* **2020**, *14*, 394−405.

(13) Lenz, M. O.; Sinclair, H. G.; Savell, A.; Clegg, J. H.; Brown, A. C.; Davis, D. M.; Dunsby, C.; Neil, M. A.; French, P. M. 3-D stimulated emission depletion microscopy with programmable aberration correction. *J. Biophotonics* **2014**, *7*, 29−36.

(14) Patton, B. R.; Burke, D.; Owald, D.; Gould, T. J.; Bewersdorf, J.; Booth, M. J. Three-dimensional STED microscopy of aberrating tissue using dual adaptive optics. *Opt. Express* **2016**, *24*, 8862−8876.

(15) Yan, W.; Yang, Y.; Tan, Y.; Chen, X.; Li, Y.; Qu, J.; Ye, T. Coherent optical adaptive technique improves the spatial resolution of STED microscopy in thick samples. *Photonics Res.* **2017**, *5*, 176−181.

(16) Wang, L.; Yan, W.; Li, R.; Weng, X.; Zhang, J.; Yang, Z.; Liu, L.; Ye, T.; Qu, J. Aberration correction for improving the image quality in STED microscopy using the genetic algorithm. *Nanophotonics* **2018**, *7*, 1971−1980.

(17) Zdankowski, P.; McGloin, D.; Swedlow, J. R. Full volume super-resolution imaging of thick mitotic spindle using 3D AO STED microscope. *Biomed. Opt. Express* **2019**, *10*, 1999−2009.

(18) Antonello, J.; Barbotin, A.; Chong, E. Z.; Rittscher, J.; Booth, M. J. Multi-scale sensorless adaptive optics: application to stimulated emission depletion microscopy. *Opt. Express* **2020**, *28*, 16749−16763.

(19) Hao, X.; Allgeyer, E. S.; Lee, D.-R.; Antonello, J.; Watters, K.; Gerdes, J. A.; Schroeder, L. K.; Bottanelli, F.; Zhao, J.; Kidd, P.; et al. Three-dimensional adaptive optical nanoscopy for thick specimen imaging at sub-50-nm resolution. *Nat. Methods* **2021**, *18*, 688−693.

(20) Booth, M. J.; Neil, M. A.; Juškaitis, R.; Wilson, T. Adaptive aberration correction in a confocal microscope. *Proc. Natl. Acad. Sci. U. S. A.* **2002**, *99*, 5788−5792.

(21) Pancholi, A.; Klingberg, T.; Zhang, W.; Prizak, R.; Mamontova, I.; Noa, A.; Sobucki, M.; Kobitski, A. Y.; Nienhaus, G. U.; Zaburdaev, V.; Hilbert, L. RNA polymerase II clusters form in line with surface condensation on regulatory chromatin. *Mol. Syst. Biol.* **2021**, *17*, No. e10272.

(22) Gao, P.; Prunsche, B.; Zhou, L.; Nienhaus, K.; Nienhaus, G. U. Background suppression in fluorescence nanoscopy with stimulated emission double depletion. *Nat. Photonics* **2017**, *11*, 163−169.

(23) Gao, P.; Nienhaus, G. U. Precise background subtraction in stimulated emission double depletion nanoscopy. *Opt. Lett.* **2017**, *42*, 831−834.

(24) Zhang, W.; Noa, A.; Nienhaus, K.; Hilbert, L.; Nienhaus, G. U. Super-resolution imaging of densely packed DNA in nuclei of zebrafish embryos using stimulated emission double depletion microscopy. *J. Phys. D: Appl. Phys.* **2019**, *52*, No. 414001.

(25) Lakshminarayanan, V.; Fleck, A. Zernike polynomials: a guide. *J. Mod. Opt.* **2011**, *58*, 545−561.

(26) Facomprez, A.; Beaurepaire, E.; Débarre, D. Accuracy of correction in modal sensorless adaptive optics. *Opt. Express* **2012**, *20*, 2598−2612.

(27) Heine, J.; Wurm, C. A.; Keller-Findeisen, J.; Schönle, A.; Harke, B.; Reuss, M.; Winter, F. R.; Donnert, G. Three dimensional live-cell STED microscopy at increased depth using a water immersion objective. *Rev. Sci. Instrum.* **2018**, *89*, No. 053701.

(28) Booth, M. J. Adaptive optical microscopy: the ongoing quest for a perfect image. *Light Sci. Appl.* **2014**, *3*, No. e165.

(29) Ji, N. Adaptive optical fluorescence microscopy. *Nat. Methods* **2017**, *14*, 374−380.

(30) Bancelin, S.; Mercier, L.; Murana, E.; Nägerl, U. V. Aberration correction in stimulated emission depletion microscopy to increase imaging depth in living brain tissue. *Neurophotonics* **2021**, *8*, No. 035001.

(31) Harke, B.; Keller, J.; Ullal, C. K.; Westphal, V.; Schönle, A.; Hell, S. W. Resolution scaling in STED microscopy. *Opt. Express* **2008**, *16*, 4154−4162.

(32) Descloux, A.; Grußmayer, K. S.; Radenovic, A. Parameter-free image resolution estimation based on decorrelation analysis. *Nat. Methods* **2019**, *16*, 918−924.

(33) Donnert, G.; Keller, J.; Medda, R.; Andrei, M. A.; Rizzoli, S. O.; Lührmann, R.; Jahn, R.; Eggeling, C.; Hell, S. W. Macromolecular-scale resolution in biological fluorescence microscopy. *Proc. Natl. Acad. Sci. U. S. A.* **2006**, *103*, 11440−11445.

(34) Sedeh, A. B.; Kobitski, A.; Dai, S.; Eroglu-Kayıkcı, S.; Nienhaus, K.; Hilbert, L.; Nienhaus, G. U. Stimulated emission double depletion nanoscopy with background correction at the single-pixel level. *Opt. Lett.* **2023**, *48*, 5791−5794.